Acta Crystallographica Section A
Foundations of Crystallography
ISSN 0108-7673

Received 31 August 2009
Accepted 14 December 2009

Non-equilibrium phonon dynamics studied by grazing-incidence femtosecond X-ray crystallography

S. L. Johnson,[a]* P. Beaud,[a] E. Vorobeva,[a] C. J. Milne,[b] É. D. Murray,[c] S. Fahy[d] and G. Ingold[a]

[a]Swiss Light Source, Paul Scherrer Institut, 5232 Villigen PSI, Switzerland, [b]Laboratoire de Spectroscopie Ultrarapide, Ecole Polytechnique Fédérale de Lausanne, 1015 Lausanne, Switzerland, [c]Department of Physics and Astronomy, Rutgers University, Piscataway, New Jersey 08854-8019, USA, and [d]Tyndall Institute and Department of Physics, University College, Cork, Ireland. Correspondence e-mail: steve.johnson@psi.ch

The timescales for structural changes in a single crystal of bismuth after excitation with an intense near-infrared laser pulse are studied with femtosecond pump-probe X-ray diffraction. Changes in the intensity and reciprocal-lattice vector of several reflections give quantitative information on the structure factor and lattice strain as a function of time, with a resolution of 200 fs. The results indicate that the majority of excess carrier energy that remains near the surface is transferred to vibrational modes on a timescale of about 10 ps, and that the resultant increase in the variance of the atomic positions at these times is consistent with the overall magnitude of lattice strain that develops.

1. Introduction

An understanding of the atomic structure of a material is usually considered a fundamental prerequisite to a study of the physical mechanisms that underlie its properties. For this purpose, X-ray crystallography is a proven, well established tool for quantitatively measuring the positions of atoms in a system with translational periodicity. Traditional methods of crystallography are, however, usually restricted to the study of *time-averaged* structures, where the timescale is at best of the order of a few milliseconds. Since the typical vibrational period of atoms is of the order of 100 fs for most materials, these methods are usually unable to study many of the structural changes that arise in a material that is not in thermodynamic equilibrium.

Recently, femtosecond pump-probe X-ray diffraction has offered a way to study these non-equilibrium structures on timescales approaching the fastest atomic vibrational periods (Rousse *et al.*, 2001; Sokolowski-Tinten *et al.*, 2001; Lindenberg *et al.*, 2005; Fritz *et al.*, 2007; Beaud *et al.*, 2007). This technique, suitable for studying quantitatively reproducible dynamics, relies on creating a time-delayed sequence of two short pulses: a 'pump' pulse that drives the material away from equilibrium and thus stimulates a dynamical response and a 'probe' pulse of X-rays that interrogates the resulting structure at a particular time by diffraction from a set of lattice planes. It is possible to trace out the structural response of a system as a function of time by repeatedly applying these two pulses to the material with different relative delays. The time resolution relies on the duration of the two pulses and on the precision of the synchronization between them. As such, progress in this area is tied intimately to the development of new sources of short-pulse hard X-rays ($\lambda \sim 1$ Å) with good synchronization to an optical laser system. Successful experiments have used the X-rays emitted by Thomson scattering from relativistic electrons (Schoenlein *et al.*, 1996), laser-produced plasmas (Rousse *et al.*, 2001; Sokolowski-Tinten *et al.*, 2001) and synchrotron-based 'slicing' of the stored electron beam (Schoenlein *et al.*, 2000; Beaud *et al.*, 2007). Much more intense pulses have been available on a test basis from a linear accelerator source (Cavalieri *et al.*, 2005), and very soon hard X-ray beamlines at X-ray free electron lasers will offer both much greater per-pulse intensity and shorter pulses (McNeil, 2009).

In this report we focus on using short-pulse X-rays from a synchrotron slicing source to study the structural response of a single crystal of bismuth after it is driven strongly out of equilibrium by the absorption of a short pulse from a near-infrared laser. Bismuth is chosen here for its strong structural response to electronic excitation, its fairly low frequency vibrational modes and its relative structural simplicity. Despite the tremendous amount of both experimental (Sokolowski-Tinten *et al.*, 2001; Fritz *et al.*, 2007; Sciaini *et al.*, 2009) and theoretical (Fahy & Reis, 2004; Murray *et al.*, 2007; Zijlstra *et al.*, 2006) work on the ultrafast dynamics of bismuth, some aspects remain controversial. For example, questions have arisen about the timescales for energy distribution and relaxation of excited carriers and how this influences the structural dynamics (Zijlstra *et al.*, 2006; Johnson *et al.*, 2009). Although a complete resolution of this particular issue will

probably require a direct experimental measurement of the time evolution of the electronic distribution, information on the structural dynamics of bismuth can help to test assumptions about how the excited carriers eventually equilibrate with the crystal lattice.

2. Overview of bismuth dynamics

At room temperature and pressure, bismuth crystallizes with a rhombohedral A7 structure: space group $R\bar{3}m$, $a = 4.7461$ Å, $\alpha = 57.23^\circ$, and Wyckoff positions $2c$ at $\pm(z, z, z)$ with $z = 0.2334$ in equilibrium (Fischer *et al.*, 1978; Cucka & Barrett, 1962). This structure is only a small distortion from a higher-symmetry simple cubic structure that would be achieved for $\alpha = 60^\circ$ and $z = 0.25$. The electronic band structure is a strong function of the magnitude of the distortion from this higher-symmetry structure: whereas the cubic structure would be a metal with a half-filled conduction band, the symmetry-breaking distortion pinches off the density of electronic states at the Fermi energy and results in a lower overall free energy (Peierls, 1991). This connection between the electronic density of states and the structure has a large impact on the ultrafast dynamics of bismuth.

2.1. Coherent optical phonon generation

Femtosecond pump-probe optical (Zeiger *et al.*, 1992; Hase *et al.*, 1998) and X-ray (Sokolowski-Tinten *et al.*, 2003; Fritz *et al.*, 2007; Beaud *et al.*, 2007; Johnson *et al.*, 2008) experiments have shown that the absorption of a near-infrared laser pulse with a duration significantly less than 300 fs results in a coherent excitation of a Γ-point A_{1g}-symmetry optical phonon mode with a very large amplitude. The resulting 'coherent phonon' is a classical-like oscillation of a vibrational mode, analogous to coherent states of the electromagnetic field (Glauber, 1963). In this case the A_{1g} coherent phonon excitation relates to an oscillation in the value of the structural parameter z about a displaced average value which is set by the level of electronic excitation created by the absorption of the pump pulse. The frequency of this oscillation decreases nearly linearly with increasing excitation fluence (Hase *et al.*, 2002). To explain these observations, models based on density functional theory (DFT) have attempted to simulate the dynamics by assuming that the absorption of the pump pulse causes an increase in the number and energy of electronic carriers, which suddenly alters the balance of the Peierls instability that controls the equilibrium value of z (Murray *et al.*, 2005; Zijlstra *et al.*, 2006). Ignoring all other phonon coordinates, we can in principle describe the potential energy of the crystal V as a function of the A_{1g} coordinate z, subject to some constraints on the excited electronic energy distribution. Before the pump laser excites the sample, there is a local minimum of $V(z)$ at $z = 0.2334$, and the A_{1g} mode frequency is proportional to $\mathrm{d}^2V/\mathrm{d}z^2$. After excitation the carriers have a different energy distribution, pushing the minimum of $V(z)$ closer to $z = 0.25$ and the mode frequency to lower values. Assuming this change happens much faster than the new vibrational period of the A_{1g} mode, the result is a large-amplitude oscillation of the atoms around the new minimum of $V(z)$ with the excited-state frequency. As the electronic excitation relaxes either by transport or by transfer of energy to other phonon modes, the quasi-equilibrium value of z will more slowly relax back to its original value without producing further oscillations. Instead this relaxation is seen in the data as a slowly changing background.

While the above DFT-based models are a useful way of thinking about the A_{1g} excitation, this picture fails to predict the generation of other coherent Γ-point modes of E_g symmetry that have been measured in optical reflectivity measurements on bismuth and similar materials (Hase *et al.*, 2002; Merlin, 1997) although Zijlstra *et al.* (2006) do discuss the coupling of such a mode to the A_{1g} coherent mode in the context of their DFT model. This is because these models ignore any coherence among excited carriers induced by the laser interaction itself, instead treating the interaction as a simple, incoherent redistribution of the energy of carriers (Merlin, 2009). As a result, there is no mechanism in these models for breaking the symmetry of the crystal. These coherences may be treated mathematically *via* an extension of the Raman tensor formalism normally applied to transparent materials (Stevens *et al.*, 2002). It is, however, not at present clear how this can be incorporated into a first-principles calculation.

2.2. Phonon squeezing

In addition to the changes in the quasi-equilibrium value of z due to electronic excitation, some DFT calculations of bismuth have predicted a 'softening' of optical and acoustic phonon branches over a large subset of the Brillouin zone (Murray *et al.*, 2007). If this change of phonon frequency happens on a timescale much faster than the period of these vibrational modes, dynamics of the *variance* of the atomic positions from their average values can result. Because these dynamics can be understood with the same mathematical treatment used in quantum optics to describe squeezed photon number states, the term 'phonon squeezing' has been used to describe this phenomenon (Garrett *et al.*, 1996; Hu & Nori, 1997; Johnson *et al.*, 2009). In essence, these dynamics are a simple consequence of any system described as a harmonic oscillator where it is possible to make fast changes to the vibrational frequency.

Fig. 1 shows a simple physical picture of what happens to the coordinate distribution corresponding to the ground state of a particular vibrational mode when the frequency of the mode is suddenly decreased. Initially, the width of the probability distribution in the phonon coordinate is static in time, corresponding to an eigenstate of a harmonic Hamiltonian defined by the initial mode frequency. If at a time $t = 0$ we suddenly change the frequency, the state of the system just after $t = 0$ will not be an eigenstate and will therefore evolve in time, resulting in changes to the width of the vibrational coordinate distribution.

More precisely, the Hamiltonian in the harmonic approximation for the vibrational modes of a crystal can be written

$$\hat{H} = \sum_{\mathbf{k}s} \hbar\omega_{\mathbf{k}s}(\hat{a}^{\dagger}_{\mathbf{k}s}\hat{a}_{\mathbf{k}s} + \tfrac{1}{2}), \tag{1}$$

where $\hat{a}^{\dagger}_{\mathbf{k}s}$ and $\hat{a}_{\mathbf{k}s}$ are the creation and annihilation operators for a phonon in the mode with wavevector $\mathbf{k}$ and branch index $\mathbf{s}$, and $\omega_{\mathbf{k}s}$ is the mode frequency. For time-independent $\omega_{\mathbf{k}s}$, this leads directly to the familiar result that any eigenstate of the Hamiltonian can be described as a direct product of eigenstates of the phonon-number operators $\hat{n}_{\mathbf{k}s} = \hat{a}^{\dagger}_{\mathbf{k}s}\hat{a}_{\mathbf{k}s}$.

We assume that at an initial time $t_{\rm eq}$ the system is in thermal equilibrium at a temperature T for an unperturbed set of values for the mode frequencies $\omega^{(0)}_{\mathbf{k}s}$. We thus describe the crystal as an admixture of phonon-number states following a Bose–Einstein distribution function, such that the average phonon number for a given mode is $n_{\mathbf{k}s} = 1/[\exp(\hbar\omega^{(0)}_{\mathbf{k}s}/k_{\rm B}T) - 1]$, where $k_{\rm B}$ is the Boltzmann constant. Now suppose that at a time $t_0 > t_{\rm eq}$ the mode frequencies change suddenly: $\omega^{(0)}_{\mathbf{k}s} \rightarrow \omega^{(1)}_{\mathbf{k}s} = \alpha_{\mathbf{k}s}\omega^{(0)}_{\mathbf{k}s}$. Since the frequencies have changed, the system is no longer in an eigenstate of the Hamiltonian and will evolve in time.

To represent mathematically the evolution of the system we will adopt the Heisenberg picture, where the time dependence is given by the operators. Accordingly, we assume a form for the time-dependent annihilation operator:

$$\hat{a}_{\mathbf{k}s}(t) = \sum_{s'}[U_{\mathbf{k}ss'}(t)\hat{a}_{\mathbf{k}s'}(t_{\rm eq}) + V_{-\mathbf{k}ss'}(t)\hat{a}^{\dagger}_{-\mathbf{k}s'}(t_{\rm eq})]. \tag{2}$$

Using

$$\mathrm{d}\hat{a}_{\mathbf{k}s}/\mathrm{d}t = (i/\hbar)[\hat{H}, \hat{a}_{\mathbf{k}s}] \tag{3}$$

and the fact that the frequencies change only at time t_0, we can partially solve for the functions $U_{\mathbf{k}ss'}(t)$ and $V_{-\mathbf{k}ss'}(t)$:

$$U_{\mathbf{k}ss'} = \begin{cases} \delta_{ss'}\exp[-i\omega^{(0)}_{\mathbf{k}s}(t-t_0)] & \text{for } t < t_0 \\ A_{\mathbf{k}ss'}\exp[-i\omega^{(0)}_{\mathbf{k}s'}(t-t_0)] & \text{for } t > t_0 \end{cases} \tag{4}$$

$$V_{-\mathbf{k}ss'} = \begin{cases} 0 & \text{for } t < t_0 \\ B_{\mathbf{k}ss'}\exp[i\omega^{(0)}_{\mathbf{k}s'}(t-t_0)] & \text{for } t > t_0 \end{cases} \tag{5}$$

where $\delta_{ss'}$ is the Kronecker delta and we have chosen $t_{\rm eq} \rightarrow t_0$.

To determine the values of $A_{\mathbf{k}ss'}$ and $B_{-\mathbf{k}ss'}$ we need to ensure the continuity at t_0 of the position

$$\hat{\mathbf{u}}^{j}(\mathbf{R}) = \frac{1}{(N)^{1/2}}\sum_{\mathbf{k}s}\left[\frac{\hbar}{2\omega_{\mathbf{k}s}(t)}\right]^{1/2}(\hat{a}_{\mathbf{k}s} + \hat{a}^{\dagger}_{-\mathbf{k}s})\boldsymbol{\varepsilon}^{j}_{\mathbf{k}s}\exp(i\mathbf{k}\cdot\mathbf{R}) \tag{6}$$

and momentum

$$\hat{\mathbf{p}}^{j}(\mathbf{R}) = -\frac{i}{N^{1/2}}\sum_{\mathbf{k}s}M^{j}\left[\frac{\hbar\omega_{\mathbf{k}s}(t)}{2}\right]^{1/2}(\hat{a}_{\mathbf{k}s} - \hat{a}^{\dagger}_{-\mathbf{k}s})\boldsymbol{\varepsilon}^{j}_{\mathbf{k}s}\exp(i\mathbf{k}\cdot\mathbf{R}) \tag{7}$$

operators for each basis atom j in the unit cell at any lattice position $\mathbf{R}$, where the $\boldsymbol{\varepsilon}^{j}_{\mathbf{k}s}$ are the normal-mode eigenvectors and M^{j} is the atomic mass. For simplicity, we will assume these eigenvectors are constant in time. The solution is then

$$A_{\mathbf{k}ss'} = \frac{1}{2}\frac{\alpha_{\mathbf{k}s}+1}{(\alpha_{\mathbf{k}s})^{1/2}}\delta_{ss'}, \tag{8}$$

$$B_{\mathbf{k}ss'} = \frac{1}{2}\frac{\alpha_{\mathbf{k}s}-1}{(\alpha_{\mathbf{k}s})^{1/2}}\delta_{ss'}. \tag{9}$$

If the eigenvectors are *not* constant, the expressions for $A_{\mathbf{k}ss'}$ and $B_{\mathbf{k}ss'}$ become more complicated and contain off-diagonal terms that serve to 'mix' the phonon branches – see Johnson *et al.* (2009) and Bartels *et al.* (2000) for details.

'Phonon squeezing' is concerned with the time dependence of $\langle\hat{Q}_{\mathbf{k}s}\hat{Q}_{-\mathbf{k}s}\rangle$, where $\hat{Q}_{\mathbf{k}s} = [\hbar/2\omega_{\mathbf{k}s}(t)]^{1/2}(\hat{a}_{\mathbf{k}s} + \hat{a}^{\dagger}_{-\mathbf{k}s})$ is the normal-mode coordinate operator. With the help of the identity $\omega_{\mathbf{k}s} = \omega_{-\mathbf{k}s}$, we find the solution

$$\begin{aligned}\langle\hat{Q}_{\mathbf{k}s}\hat{Q}_{-\mathbf{k}s}\rangle &= \frac{\hbar}{4\omega^{(0)}_{\mathbf{k}s}}\left[\left(1+\frac{1}{\alpha^{2}_{\mathbf{k}s}}\right) + \left(1-\frac{1}{\alpha^{2}_{\mathbf{k}s}}\right)\cos 2\alpha_{\mathbf{k}s}\omega^{(0)}_{\mathbf{k}s}(t-t_0)\right] \\ &\quad\times(2n_{\mathbf{k}s}+1).\end{aligned} \tag{10}$$

The time dependence is characterized by an oscillation at twice the frequency of the normal mode after excitation. This oscillation in the quadrature of the normal-mode coordinate (and its corresponding canonical momentum) is what is meant here by 'phonon squeezing'. Note that if we start with a sufficiently cold crystal such that $n_{\mathbf{k}s} \rightarrow 0$ it is possible to use this effect to temporarily push $\langle\hat{Q}_{\mathbf{k}s}\hat{Q}_{-\mathbf{k}s}\rangle$ below the zero-point motion 'limit' of $\hbar/2\omega_{\mathbf{k}s}$ in a manner analogous to vacuum-state squeezing of the electromagnetic field in quantum optics.

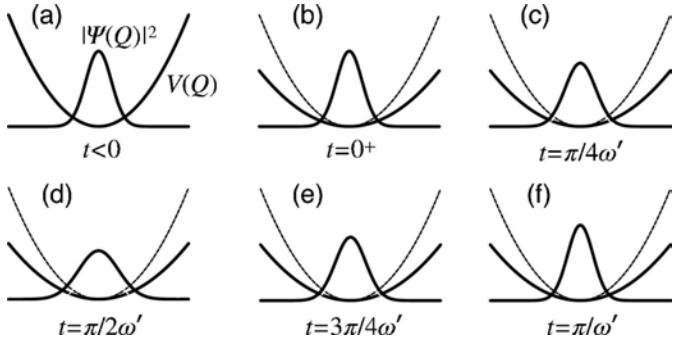

Figure 1
Wavepacket evolution of a squeezed state, depicting a squeezing of the ground state of a single vibrational mode. (*a*) Initially, the state corresponds to the ground state of a simple harmonic oscillator with potential energy $V(Q) = M\omega^2/2$ with mass M and frequency ω. The variance of the vibrational coordinate Q is $\langle Q^2\rangle = \hbar/2M\omega$. (*b*) At a time $t = 0$, the frequency of the oscillator suddenly decreases: $\omega \rightarrow \omega' = \alpha\omega$, where $\alpha < 1$. The wavepacket remains initially the same, but after $t = 0$ the wavefunction does not correspond to an eigenstate of the potential and starts with a variance in Q lower than that of the ground state of the modified potential. (*c*) At a times $0 < t < \pi/2\omega'$, the wavepacket expands in position space. (*d*) At $t = \pi/2\omega'$ the variance $\langle Q^2\rangle$ reaches a maximum value of $\hbar/2M\alpha^2\omega$. Also at this time, the corresponding variance in the momentum reaches a minimum. (*e*) At times between $t = \pi/2\omega'$ and $t = \pi/\omega'$ the coordinate variance decreases. (*f*) At $t = \pi/\omega'$ the state returns to the condition in panel (*b*) and the cycle repeats with angular frequency $2\omega'$.

2.3. Lattice heating

The foregoing discussion of phonon squeezing touched only on structural dynamics arising from suddenly altering the frequencies of vibrational modes. In addition to this, electron–phonon scattering processes will transfer energy from the highly excited electrons to the vibrational modes. Both these effects result in a non-thermal energy distribution of phonons which must eventually relax *via* anharmonic phonon–phonon interactions. Insofar as these interactions involve $q = 0$ acoustic modes, these interactions will lead to an average strain. The timescale for phonon equilibration is difficult to estimate from current data, but it is known that the coherent A_{1g} mode decays on timescales ranging from about 1–10 ps, depending on the excitation fluence and crystal temperature (Hase *et al.*, 2002; Misochko *et al.*, 2006). This suggests that attempting to define a 'lattice temperature' on these timescales is problematic, and effects from a non-Bose–Einstein distribution of phonons may be important.

3. Elements of femtosecond X-ray diffraction

3.1. Probe depth: absorption and extinction

In a grazing-incidence geometry, where the incidence angle is only slightly larger than the critical angle for total external reflection, the effective probe depth of X-ray diffraction is controlled by two physically distinct mechanisms: absorption and extinction. The relative importance of these mechanisms depends in general on the intrinsic properties of the crystal, the efficiency of the particular diffraction peak under investigation, the angle of incidence for the X-rays, and the size and distribution of individual domains in the crystal.

We first consider the situation depicted in Fig. 2, where a monochromatic X-ray beam with frequency ω incident from vacuum enters the planar surface of a semi-infinite, perfect crystal with a dielectric susceptibility χ_0. The susceptibility χ_0 is a complex number related to the electron density ρ_e and the X-ray absorption coefficient μ by

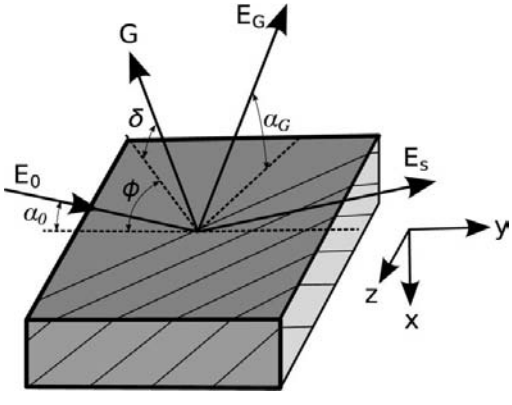

Figure 2
Schematic of the X-ray diffraction geometry for non-coplanar grazing incidence from lattice planes with reciprocal-lattice vector **G**. The incident beam ($\mathbf{E}_0$) enters the sample at a glancing angle α_0, and two beams leave the surface: a specular reflected beam ($\mathbf{E}_s$) and a diffracted beam ($\mathbf{E}_G$).

$$\chi_0 = \chi_0' + i\chi_0'' = -\frac{4\pi r_e}{k^2}\rho_e + i\frac{2\mu}{k}, \tag{11}$$

where $k = \omega/c$ is the magnitude of the incident wavevector, c is the speed of light in vacuum and r_e is the classical electron radius. We assume that the geometry of the crystal and beam are such that exactly one set of crystal planes with reciprocal-lattice vector **G** nearly satisfy the Bragg condition, and that the grazing-incidence angle α_0 is small but the exit angle α_G of the diffracted beam is large compared to the critical angle for external reflection $\alpha_c = (\chi_0')^{1/2}$. The electric field outside the crystal ($x < 0$) at a time t is

$$\begin{aligned}\mathbf{E}_v(\mathbf{r}, t) = \big\{\big[\mathbf{E}_0 \exp(ik\gamma_0 x) + \mathbf{E}_s \exp(-ik\gamma_0 x)\big] \exp(i\mathbf{k}_{||} \cdot \mathbf{r}_{||}) \\ + \mathbf{E}_G \exp(ik\gamma_G x) \exp[i(\mathbf{k} + \mathbf{G})_{||} \cdot \mathbf{r}_{||}]\big\} \exp(-i\omega t),\end{aligned} \tag{12}$$

where **k** is the incident wavevector, $\gamma_0 = \sin\alpha_0$, $\gamma_G = -\sin\alpha_G$ and the subscript $||$ denotes the projection of a vector onto the $x = 0$ plane. The vector $\mathbf{E}_0$ represents the amplitude and polarization of the incident beam, while $\mathbf{E}_s$ is the specular reflected beam and $\mathbf{E}_G$ is the diffracted beam that exits the crystal. The value of γ_G (and therefore α_G) is set by the condition that the magnitude of the wavevector for the diffracted beam is the same as for the incident beam:

$$\gamma_G = -[(\gamma_0 - \psi)^2 + \zeta]^{1/2}, \tag{13}$$

where

$$\zeta = 4\sin\theta_B(\sin\theta_B - \cos\phi\cos\delta\cos\alpha_0 - \sin\delta\sin\alpha_0) \tag{14}$$

is the deviation from the Bragg condition, $\psi = 2\sin\theta_B \sin\delta$, θ_B is the Bragg angle, δ is the angle between **G** and the surface, and ϕ is the angle between the projection of **G** onto the surface and the negative y axis. Inside the crystal the fields are

$$\begin{aligned}\mathbf{D}(\mathbf{r}, t) = \big\{\mathbf{D}_0 \exp(iku x) \exp(i\mathbf{k}_{||} \cdot \mathbf{r}_{||}) \\ + \mathbf{D}_G \exp[ik(u - \psi)x] \exp[i(\mathbf{k} + \mathbf{G})_{||} \cdot \mathbf{r}_{||}]\big\} \exp(-i\omega t).\end{aligned} \tag{15}$$

Here the $\mathbf{D}_0$ term is a wave going deeper into the crystal and the $\mathbf{D}_G$ term is the diffracted wave that moves back toward the surface. As shown by Aleksandrov *et al.* (1984), the possible values for the quantity u are determined by roots of the cubic dispersion equation

$$(u^2 - {\gamma_0}^2 - \chi_0)[u - \psi + ({\gamma_G}^2 + \chi_0)^{1/2}] = \frac{P^2 \chi_G \chi_{\overline{G}}}{2|\gamma_G|} \tag{16}$$

where χ_G and $\chi_{\overline{G}}$ are the Fourier components of the susceptibility for **G** and $-\mathbf{G}$, respectively, and $P = 1$ for σ polarization and $P = \cos 2\theta_B$ for π polarization. In general equation (16) yields three possible values for u, one with $\mathrm{Im}[u] > 0$ and two with $\mathrm{Im}[u] < 0$. The latter two roots, when inserted into equation (15), correspond to waves that grow exponentially with depth into the crystal. Since these are unphysical, we discard them and we are left with only one possibility for u. The distance from the surface L where the fields inside the crystal are attenuated by a factor of $1/e$ is then simply $L = 1/k\mathrm{Im}[u]$.

To isolate the effect of photoabsorption on L, we take the limit $|\chi_G| \rightarrow 0$ so as to make the effect of extinction negligible. In this case equation (16) is easily factored, and the roots are

$$u_{1,2} = \pm(\gamma_0{}^2 + \chi_0)^{1/2}, \tag{17}$$

$$u_3 = \psi - (\gamma_G{}^2 + \chi_0)^{1/2}. \tag{18}$$

Of these, only u_1 has a positive imaginary component. Thus,

$$L_{\rm abs} = \frac{1}{k{\rm Im}[u_1]} = \frac{1}{k}\left(\frac{2}{-\gamma_0^2 - \chi_0' + \left[(\gamma_0^2 + \chi_0')^2 + (\chi_0'')^2\right]^{1/2}}\right)^{1/2} \tag{19}$$

is the contribution of photoabsorption to the attenuation of the wavefield inside the crystal. Note that this depends only on the X-ray wavelength, the incidence angle and χ_0.

In our experiments the orientation of **G** is non-collinear with **n**, making it possible to use a rotation ϕ about the sample normal to adjust the angle between the incident beam and the lattice planes. Fig. 3 shows the dependence of L on $\Delta\phi = \phi - \phi_{\rm B}$ for the (111) planes in a single crystal of bismuth with a (311) surface, where $\phi_{\rm B}$ is the value of ϕ where the diffraction is maximized. Here we keep $\alpha_0 = 0.5^\circ$. Although under these conditions L does not vary strongly across the diffraction peak, there is a noticeable minimum near the conditions of highest diffraction efficiency. This is the contribution of extinction to the penetration depth, where the diffracted beam acts to attenuate the incoming beam. Interestingly, the behavior of L is asymmetric, and even has a small maximum at $\Delta\phi = 0.2^\circ$. This asymmetry is a consequence of small differences in the effective absorption coefficient seen by the small standing wave component of the field inside the crystal that shifts phase across the ϕ-scan (Batterman & Cole, 1964). Fig. 4 shows both the minimum value of the penetration depth $L_{\rm min}$ and $L_{\rm abs}$ as a function of incidence angle α_0. At low values of α_0 these are very close and extinction may be neglected altogether in order to simplify analysis.

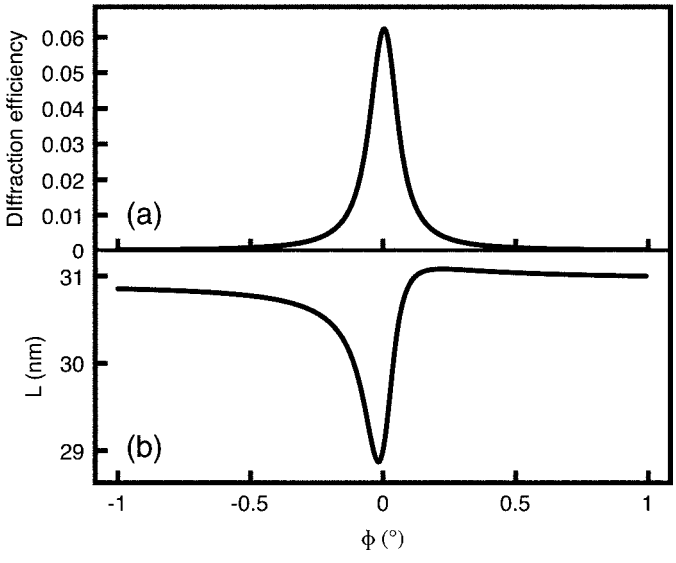

Figure 3
Calculated X-ray diffraction efficiency (*a*) and field penetration depth L (*b*) for the (111) Bragg reflection in (311)-oriented Bi as a function of rotation angle $\Delta\phi$ about the surface normal, for an incidence angle $\alpha_0 = 0.5^\circ$. Only the results for the σ-polarized component are shown. The results for π polarization are qualitatively similar but show smaller changes in L due to the lower value of the polarization factor P.

3.2. Dynamics of the reciprocal lattice: coherent acoustic phonons

Acoustic phonons describe the low-energy structural excitations of a crystal lattice with a frequency depending nearly linearly on the crystal momentum **q** as $|\mathbf{q}| \rightarrow 0$. As shown by Thomsen *et al.* (1986) for picosecond laser heating, an instantaneous increase in isotropic stress near the surface will result in a strain wave (coherent longitudinal acoustic phonons) due to the elastic response of the material. This strain wave starts at the surface and moves into the crystal at a the speed of sound v. Non-isotropic stresses or elastic tensors may also induce coherent transverse acoustic strain.

In terms of the structure of the crystal, low-wavevector coherent acoustic modes cause local changes in the reciprocal lattice of the crystal. In the formalism of the preceding section, this is equivalent to changes in the reciprocal-lattice vector **G** for various diffraction planes. In our diffraction experiment, it is possible to track spatially averaged changes in the reciprocal-lattice vector **G** by measuring time-dependent changes in the direction of the diffracted beam $\mathbf{k}_G$ and/or the diffraction efficiency as a function of sample rotation angle ϕ. Assuming the transverse length scales of the sample and excitation are large (>100 µm), the relevant timescale for changes in **G** is set by the smaller of the X-ray probe depth L and the laser excitation depth $L_{\rm ex}$; for a 20 nm depth, the relevant timescale would be 10 ps for $v \simeq 2000$ m s^{-1}. At times significantly earlier than this, we expect little change in **G** over the probed volume.

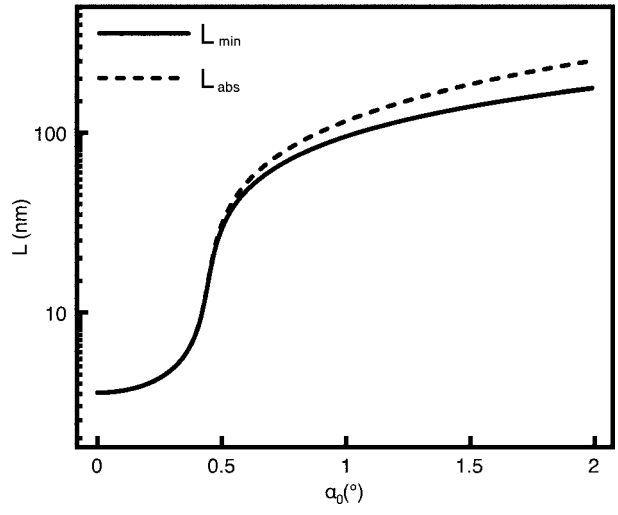

Figure 4
The minimum field penetration depth $L_{\rm min}$ for the (111) reflection and the field penetration depth $L_{\rm abs}$ far from a Bragg reflection in (311)-oriented Bi as a function of incidence angle α_0. As in Fig. 3, only the results for the σ-polarized component are shown.

3.3. Dynamics of the diffracted intensity: coherent optical phonons and disorder

The intensity of the diffracted beam in equation (12) can be determined in the usual way by solving for boundary conditions at the crystal surface. As shown by Aleksandrov *et al.* (1984), for our geometry the result is

$$I_G = -\frac{\gamma_0}{\gamma_G}\left|\frac{\chi_G}{(u+\gamma_0)(u-\psi-\gamma_G)}\right|^2, \qquad (20)$$

where we recall that $\gamma_G = -\sin\alpha_G < 0$. If we assume that u does not depend strongly on χ_G (equivalent to assuming $L \simeq L_{\rm abs}$), the diffracted intensity is proportional to $|\chi_G|^2$ as it is in the simple kinematic theory of diffraction. Under the assumption that the electronic density is localized at the positions of the basis atoms of the unit cell, we can write

$$\chi_G = \frac{4\pi r_{\rm e}}{k^2 V} S_G, \qquad (21)$$

where V is the unit-cell volume and the structure factor

$$S_G = \sum_j f_j \exp(i\mathbf{r}_j \cdot \mathbf{G}) \exp[-\langle(\hat{\mathbf{u}}^j \cdot \mathbf{G})^2\rangle/2] \qquad (22)$$

depends on the atomic form factor f_j and the relative position $\mathbf{r}_j$ of the jth basis atom in the crystal unit cell. The Debye–Waller term $\exp[-\langle(\hat{\mathbf{u}}^j \cdot \mathbf{G})^2\rangle/2]$ expresses the decrease in S_G due to incoherent atomic vibrations in the direction of $\mathbf{G}$.

Time-dependent changes in S_G due to spatially homogeneous structural dynamics in the crystal can enter through the basis-atom positions $\mathbf{r}_j$ (coherent optical phonons) and/or through the Debye–Waller factor. In the specific case of the bismuth structure with two identical basis atoms, we can simplify equation (22) to

$$S_G = 2f \cos(\mathbf{r} \cdot \mathbf{G}) \exp[-\langle(\hat{\mathbf{u}} \cdot \mathbf{G})^2\rangle/2], \qquad (23)$$

where $f = f_1 = f_2$, $\langle(\hat{\mathbf{u}} \cdot \mathbf{G})^2\rangle = \langle(\hat{\mathbf{u}}^1 \cdot \mathbf{G})^2\rangle = \langle(\hat{\mathbf{u}}^2 \cdot \mathbf{G})^2\rangle$ and $\mathbf{r} = \mathbf{r}_1 = -\mathbf{r}_2$.

Under the 'kinematic' assumption $L \simeq L_{\rm abs}$, we can then approximate the diffracted intensity as

$$I_G \simeq I_G^{(0)} \frac{\cos^2(\mathbf{r} \cdot \mathbf{G})}{\cos^2(\mathbf{r}_0 \cdot \mathbf{G})} \exp[-\Delta\langle(\hat{\mathbf{u}} \cdot \mathbf{G})^2\rangle], \qquad (24)$$

where $I_G^{(0)}$ is the initial intensity and $\mathbf{r}_0$ is the initial value of $\mathbf{r}$. For the (111) Bragg reflection, $\mathbf{r} \cdot \mathbf{G} = 6\pi z$, and so the coherent dynamics of the A_{1g} mode lead to a response in I_G. This is also true for the higher-order (222) planes where $\mathbf{r} \cdot \mathbf{G} = 12\pi z$. For planes perpendicular to (111), the intensity is sensitive to impulsively stimulated E_g coherent modes only to second order in $\mathbf{r} - \mathbf{r}_0$, since $\mathbf{r}_0 \cdot \mathbf{G} = 0$. Diffraction from these planes is therefore relatively more sensitive to changes in the Debye–Waller factor.

4. Experimental description

The experimental setup for performing grazing-incidence femtosecond X-ray diffraction consists of several components. The sample is a single crystal of bismuth, with a surface normal along the [311] direction (in rhombohedral coordinates). To excite the sample, we use the output from a commercially available Ti:Al_2O_3-based regenerative amplifier (800 nm, 115 fs, 1 kHz) focused to an elliptical spot with dimensions 750 × 4000 µm at a 10° grazing-incidence angle. The polarization of the pump beam was p-polarized to maximize absorption in the sample.

To probe the X-ray diffraction from the excited sample, we generate 140 ± 30 fs duration X-rays from a synchrotron using the electron-beam slicing method (Schoenlein *et al.*, 2000; Beaud *et al.*, 2007). Briefly, a regenerative-amplifier-based laser system creates 50 fs duration pulses of light with wavelength 800 nm at a rate of 2 kHz synchronized to both the synchrotron storage ring and to the pump laser. These pulses are timed to co-propagate with the electron beam as it passes through a wiggler tuned to near resonance with the frequency of the laser field. This causes an energy modulation of a short time 'slice' of the electron beam, which is subsequently separated from the other electrons by energy-dispersive electron optics. This separated slice of electrons then generates X-rays when passing through an in-vacuum undulator. These X-rays are first collimated vertically and brought to a weak 250 µm focus at the sample position by a grazing-incidence toroidal mirror. Approximately 30 cm before the sample, a single elliptically bent mirror focuses the beam vertically to a size of 7 µm at the sample position. An Mo/B_4C multilayer mirror then deflects the beam horizontally just before the beam hits the sample, serving to weakly monochromatize the X-rays at a phonon energy of 7.1 keV and a bandwidth of 1.3%.

The incidence angle of the X-rays on the sample is measured by monitoring the deflection of the specular component of the surface reflection of X-rays from the sample. The diffracted X-rays are detected using a large-area 10 × 10 mm avalanche photodiode (APD) with a stack of three 25 µm Be windows in place to block contributions from pump laser scatter. The current from the APD is then sent through a fast transimpedance amplifier to a gated voltage integrator. The integrated APD current from each sliced X-ray pulse (arrival rate 2 kHz) is individually measured and stored. Note that since the X-rays arrive at twice the repetition rate of the pump laser, the measurements alternate between taking measurements of the excited and unexcited samples, provided the sample relaxes within 500 µs. This allows us to normalize out sources of noise connected with slower timescale fluctuations in the slicing interaction. In addition, we also measure and store the integrated signal at one synchrotron round trip (960 ns) *earlier* than the arrival of the sliced beam. This signal serves as a measure of the 'halo' of incompletely relaxed electrons in the storage ring that has been created by previous interactions with the slicing laser (Holldack *et al.*, 2006; Beaud *et al.*, 2007). This halo contribution leads to a roughly 70 ps full-width-at-half-maximum (FWHM) background to the slicing signal with an integrated intensity of approximately 10% of the total measured signal. For the very short timescale data (<5 ps) the halo contribution to the pump-probe signal is approximately constant and we can simply subtract it out; for

longer timescales, however, this background does contribute to the measured data.

5. Results

The experimental results are most easily divided into two parts, differentiated primarily by timescale. What we will call 'fast dynamics' on times earlier than about 3 ps reflect behavior in the regime where the strain and volume are constant, and the sample is far from local thermal equilibrium. The 'slow dynamics' show the onset of strain and thermalization, followed by thermal diffusion that drives the near-surface temperature back down to its original value.

5.1. Short timescale behavior: A_{1g} and Debye–Waller dynamics

Fig. 5 shows the time dependence of the diffracted intensity over 5 ps from the (111), (222) and $(10\bar{1})$ lattice planes for an absorbed excitation fluence of 1.4 ± 0.3 mJ cm^{-2} and an X-ray incidence angle of 0.45°. The halo contribution has been assumed to be constant and is subtracted out from these data. Oscillations from the coherently excited A_{1g} mode are clearly visible in the (111) and (222) data. In addition, we see an overall drop in the diffracted intensity for the $(10\bar{1})$ data that we can attribute to the Debye–Waller factor. Using equation (24) we can extract from these data the dynamics of z and $\langle(\hat{\mathbf{u}}\cdot\mathbf{h})^2\rangle$ for $\mathbf{h} = \mathbf{G}/|\mathbf{G}|$. Figs. 6 and 7 show the results of this decomposition. Note that previous work (Beaud *et al.*, 2007; Johnson *et al.*, 2008) has inferred z dynamics by assuming that the Debye–Waller contribution to the (111) data is negligible. As shown quantitatively here, this assumption is justified since the magnitude of **G** for these planes is quite small, leading to an overall error in Δz of the order of just 5%. The current treatment, however, has the advantage of being able to extract quantitative information on the dynamics of the variance in the [111] direction.

From Fig. 6, the dynamics of z show the displacive excitation of the A_{1g} mode caused by an electronically induced shift in $z_{\rm eq}$, the quasi-equilibrium value of z. The solid line shows a fit to a simple model of displacive excitation where we assume a constant phonon frequency, a linear damping coefficient and an exponential relaxation of $z_{\rm eq}$ back to its original value (Zeiger *et al.*, 1992). As with all the model calculations shown here, the curve has been convoluted with a Gaussian with 200 fs FWHM to take the time resolution into account. The fit gives a frequency of 2.51 ± 0.03 THz, an oscillation damping time $\tau_{\rm osc} = 0.79 \pm 0.14$ ps, and a $z_{\rm eq}$ relaxation time of $\tau = 2.94 \pm 0.09$ ps.

Since DFT calculations have indicated that the value of $z_{\rm eq}$ is approximately linear with the excited carrier density (averaged over one cycle of oscillation), we can take the value of τ as an estimate of the time for the average number of excited carriers to decay. This decay in the average number of carriers is likely to be due to a combination of carrier diffusion (which moves carriers deeper into the crystal) and transfer of electronic energy to the vibrational modes *via* incoherent electron–phonon interactions. A more detailed study (Johnson *et al.*, 2008) of the behavior of z over this time interval for a slightly lower absorbed fluence of 1.1 mJ cm^{-2} was able to use measurements at different X-ray incidence to obtain depth resolution, giving the ability to distinguish between losses from carrier transport and from energy transfer to the lattice. Based on a fit to a somewhat complicated model of carrier–carrier and carrier–phonon interactions, this work estimated an effective diffusion coefficient $D = 2.3 \pm 0.3$ cm^2 s^{-1} and an electronic energy decay time of $\tau_{\rm el} = 7.6 \pm 0.6$ ps. For deep probe depths these data also indicate an *increase* in $z_{\rm eq}$ over the first oscillation cycle, which was interpreted as carrier–carrier interaction that acted to increase the number of carriers in the crystal over this time

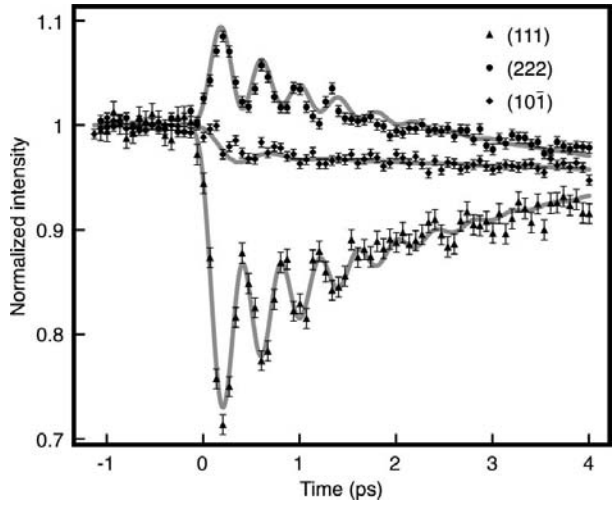

Figure 5
Normalized diffraction from the (111), (222) and $(10\bar{1})$ planes as a function of time after laser excitation. The solid lines show the results of the fits discussed in the text.

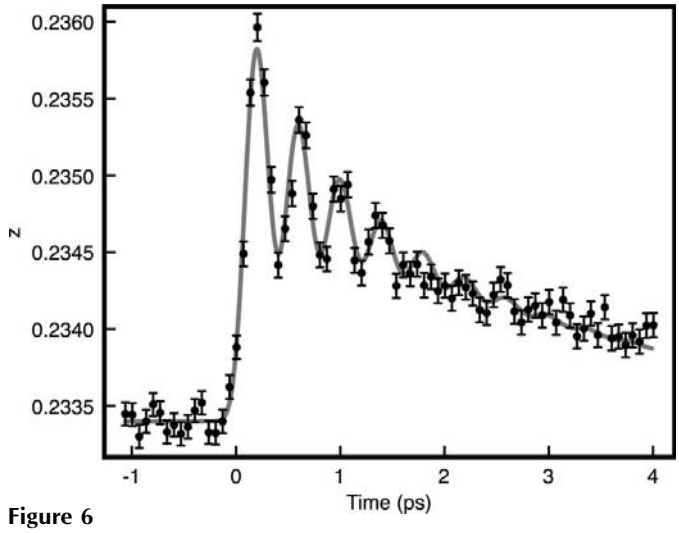

Figure 6
Dynamics of the atomic position parameter z extracted from the data shown in Fig. 5. The solid line is the result of a fit to a simple model of displacive excitation with a constant phonon frequency, as discussed in the text.

frame, possibly due to impact ionization. Although this interpretation should be confirmed with a more direct measurement of the time dependence of the carrier distribution, it is intriguing. This increase in z_{eq} is not normally observed in optical reflectivity experiments since near the surface it appears to be at least partially cancelled by carrier diffusion.

The dynamics of $\langle(\hat{\mathbf{u}}\cdot\mathbf{h})^2\rangle$ in Fig. 7 in both directions show a prompt increase in the atomic disorder after excitation, followed by a much slower, nearly linear increase. There is no large quantitative difference between the two directions from our data. As a supplement to these data, Fig. 8 shows somewhat higher quality data for the $[11\bar{2}]$ direction taken in a vacuum sample environment at a similar fluence level at two different initial sample temperatures (Johnson *et al.*, 2009). The data set at room temperature shows clear evidence of phonon squeezing as discussed in §2.2, appearing as a small, quickly damped oscillation with a period of approximately 750 fs that accompanies the initial increase.

In terms of the theory developed in §2.2, we can calculate (under the simplifying assumption of constant eigenvectors) the direction-projected atomic variance

$$\langle(\hat{\mathbf{u}}^j\cdot\mathbf{h})^2\rangle = (1/N)\sum_{\mathbf{k}s}\langle Q_{\mathbf{k}s}Q_{-\mathbf{k}s}\rangle|\boldsymbol{\varepsilon}^j_{\mathbf{k}s}\cdot\mathbf{h}|^2. \qquad (25)$$

As equation (25) shows, the atomic variance along a particular direction is the sum of phonon-squeezing contributions from all different vibrational modes. The fact that many different frequencies contribute to the measured signal explains the fast damping of the observed oscillations. As a very simple, first-order approximation of the effects of electronic excitation on the phonon dispersion, we will assume that $\alpha_{\mathbf{k}s} = \alpha$ is independent of the phonon wavevector $\mathbf{k}$ and branch s. By using the ground-state DFT calculations from Murray *et al.* (2007) to get the eigenvectors and initial frequencies, we use equation (25) to fit to the data, varying α as a fit parameter. In order to fit the nearly linear, slow increase in the atomic variance at later times we have added to this model a term of the form bt, where we also allow the slope b to vary as a fit parameter. The solid lines in Figs. 7 and 8 show the results of the fit, where we have forced use of the same parameters to describe the [111] and $[10\bar{1}]$ directions since these data sets share the same excitation level. The data in Fig. 7 are fitted well by $\alpha = 0.858 \pm 0.004$ and $b = (4.5 \pm 0.5) \times 10^{-4}$ Å^2 ps^{-1}, whereas the data of Fig. 8 yield $\alpha = 0.8793 \pm 0.0013$ and $b = (8.0 \pm 0.2) \times 10^{-4}$ Å^2 ps^{-1} for $T = 300$ K and $\alpha = 0.889 \pm 0.003$ and $b = (7.4 \pm 0.4) \times 10^{-4}$ Å^2 ps^{-1} for $T = 170$ K. The fit parameters are quite similar, suggesting that the relevant vibrational-mode frequencies soften (decrease) at these excitation fluences by about 11–14%.

5.2. Heating and lattice strain: long timescale behavior

Over longer timescales, the development of strain from coherent acoustic phonons leads to a change in **G** and a corresponding shift in the value of ϕ_B. To measure this, we performed ϕ-scans of the diffraction efficiency at room temperature for the (111) and $(11\bar{2})$ reflections at different fixed pump-probe delay times of 3, 6.4 and 35 ps, as well as scans of the pump-probe delay at three different values of ϕ at and around the exact Bragg condition. For all these measurements the X-ray incidence angle was fixed at $\alpha_0 = 0.5^\circ$ and the absorbed laser fluence was 1.2 ± 0.2 mJ cm^{-2}. Owing to the large bandwidth of the X-rays, we observed that for a given reflection the shape of the intensity profile as a function of ϕ was unchanged for different pump-probe delay times, with only the overall intensity and shift of the Voigt-shape profile changing with the delay time. Using equation (14) we can determine ϕ_B in terms of θ_B and the angle δ between **G** and the surface:

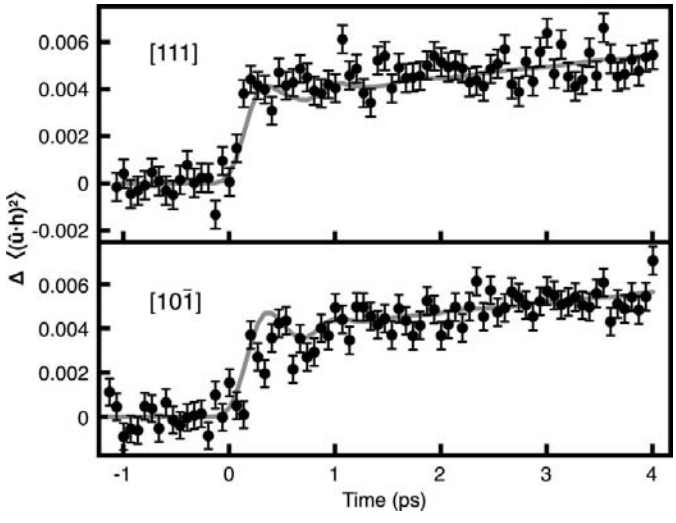

Figure 7
Dynamics of the atomic variance projected along the [111] and $[10\bar{1}]$ directions extracted from the data shown in Fig. 5. The solid line is the result of the fit discussed in the text.

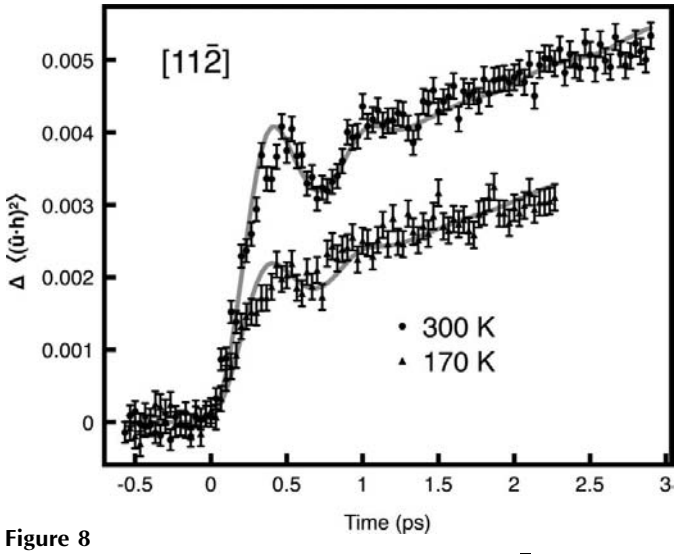

Figure 8
Dynamics of the atomic variance projected along the $[11\bar{2}]$ direction from a different experimental run (Johnson *et al.*, 2009) at two different temperatures: 300 and 170 K. The solid lines are the result of the fit discussed in the text.

$$\cos\phi_B = \frac{\sin\theta_B - \sin\delta\sin\alpha_0}{\cos\delta\cos\alpha_0}. \quad (26)$$

If we assume that the elastic properties of bismuth are isotropic, by symmetry we can argue that the lattice strain should affect only the component of **G** normal to the surface. In reality, the elastic properties of bismuth at room temperature are not isotropic: for example, the difference in longitudinal sound velocities ranges from 1.97 km s^{-1} along the [111] direction to about 2.55 km s^{-1} in the plane perpendicular to [111] (Eckstein, 1960). These velocities are, however, relatively similar, so we proceed with an approximation of isotropy while keeping in mind that there may be small non-normal changes in **G** due to the anisotropy of the elastic tensor.

Let **n** be the surface normal of the crystal. Taking $\eta = (\Delta\mathbf{G}\cdot\mathbf{n})/(\mathbf{G}\cdot\mathbf{n})$ as the normal component of lattice strain averaged over the probe depth, from equation (26) we obtain

$$\frac{d\eta}{d\phi_B} = -\frac{\sin\phi_B}{\sin\theta_B\tan\delta(1+\sin\delta)}, \quad (27)$$

which relates small shifts in ϕ_B to η for an assumed homogeneous probe volume. Fig. 9 shows the results of calculating η as a function of time, based on a fit of the measured ϕ profile shape to the three values of ϕ used in the pump-probe delay scans. This analysis gives only an approximation of η and may be inaccurate at times when the strain is highly inhomogeneous. For both reflections there is no measurable change in η until after 5 ps. There is an increase in strain at 5–20 ps that is likely to correspond to a strain wave moving across the probe depth, followed by a slower relaxation out to beyond 200 ps that is probably due to a cooling of the lattice from thermal diffusion. For both reflections the calculated strain is quantitatively similar. The precise timescale of the increase in strain may be affected by the assumption of homogeneity in deriving equation (27); a more accurate analysis would require additional data and calculation of the diffracted intensity directly from a parameterized model of the strain wave.

We can also extract from the fits the long-time behavior of the integrated intensity of diffraction from each reflection. Because the small magnitude of the (111) reciprocal-lattice vector makes diffraction from these planes relatively insensitive to the Debye–Waller factor, the (111) data show a nearly complete recovery of the initial intensity after about 20 ps. For the $(11\bar{2})$ data we have transformed this into the time dependence of $\langle(\hat{\mathbf{u}}\cdot\mathbf{G})^2\rangle$, shown in Fig. 10. We see at very early times the fast increase from the softening of the phonon frequencies, followed by a steady increase in the variance until about 10 ps, when the variance begins to decrease again and relax to its initial value sometime after the window of the measurement. This decrease is probably again due to diffusion of vibrational energy away from the probe volume. Although the crystal may not be in true thermodynamic equilibrium at the peak time of 10 ps, it is possible to estimate an 'effective' temperature assuming this is the case. Since the starting temperature is well above the Debye temperature of 120 K, the variance will scale linearly with temperature. Using a value of 0.0143 Å^2 as the equilibrium value at 300 K (Narayana & Krishna, 2005), the observed 0.005 Å^2 increase would correspond to a temperature increase of approximately 100 K.

As a check of consistency, we can try to use this value of the effective temperature to calculate the corresponding normal strain. Since the strain forms dynamically in response to the stress as a strain wave that begins at the crystal surface, we would expect a delay of the strain response of the order of L/v = 13 ps, where L = 30 nm is the probe depth and v =

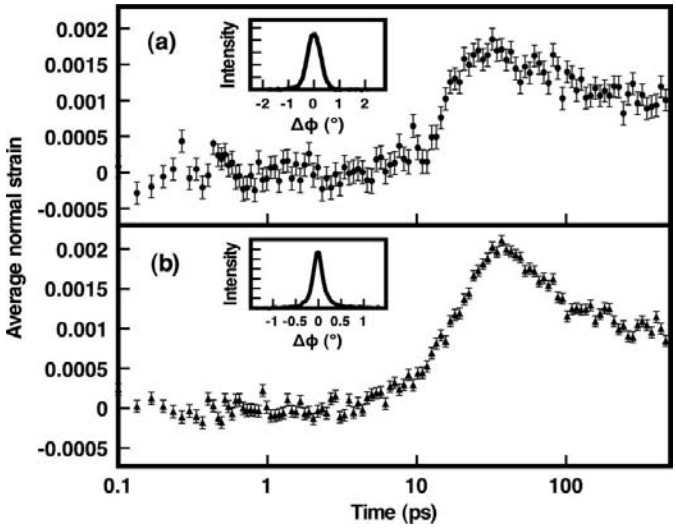

Figure 9
Normal component of the lattice strain estimated from the changes in ϕ_B determined from a fit to diffraction measurements at three different values of the sample rotation ϕ. The data shown in (*a*) are extracted from the $(11\bar{2})$ reflection and the data in (*b*) are from the (111) reflection. The insets show the diffracted intensity as a function of $\Delta\phi$ at 3 ps for each reflection. The calculation of the strain assumes the strain is homogeneous and approximates the elastic properties of bismuth as isotropic; corrections for these assumptions may alter the shape of the initial rise and explain the small differences between the curves.

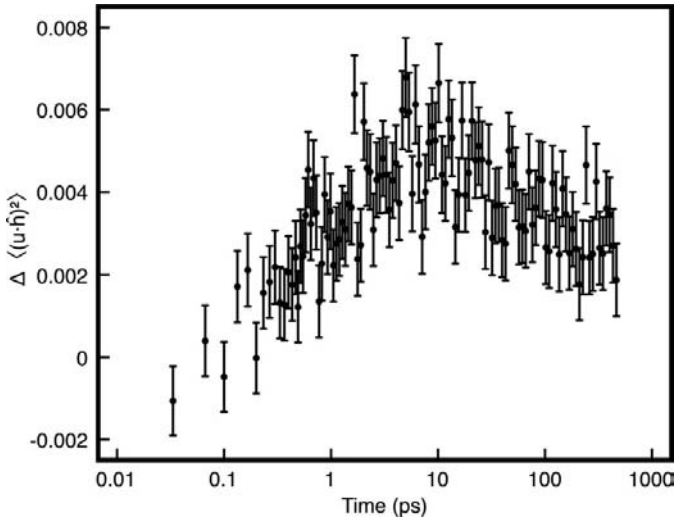

Figure 10
Long timescale behavior of $\langle(\hat{\mathbf{u}}\cdot\mathbf{G})^2\rangle$ for the $[11\bar{2}]$ direction at 300 K, extracted from diffraction measurements at three different values of sample rotation ϕ.

2.35 km s^{-1} is the longitudinal sound velocity averaged over all directions. On timescales exceeding the time for such a strain wave to propagate across the probe depth, the normal strain resulting from such a temperature increase can be estimated (Thomsen *et al.*, 1986) as

$$\eta = \frac{B\beta\Delta T}{\rho v^2}, \tag{28}$$

where ρ = 9.8 g cm^{-3} is the density, B = 33 GPa is the bulk modulus (Eckstein, 1960) and $\beta = 4.0 \times 10^{-5}$ K^{-1} is the volume thermal expansion coefficient (White, 1972). With ΔT = 100 K we obtain a value of $\eta = 0.0024$ which is close to the peak values in Fig. 9 at around 20 ps, delayed from the peak in Fig. 10 by about L/v. The overall magnitude of the strain derived from the data thus seems consistent with that of the atomic position variance. This, however, does not necessarily imply that the system is indeed in thermal equilibrium, since there is no way to know from these data how the energy in the phonon modes is actually distributed.

6. Conclusions

Sudden high-level excitation of bismuth results in a multitude of structural responses. First, the electronic excitation itself causes significant changes in the interatomic potential surface. This results in the generation of an A_{1g} coherent phonon and in 'squeezing' dynamics of the atomic variance due to a sudden change in frequency of the vibrational modes. These effects of vibrational-mode softening appear from the existing data to produce changes in the atomic position variance of approximately equal magnitude in all the directions probed, which is consistent with an average frequency decrease of 11–14% for the excitation fluences we have applied.

At later times, electron transport acts to move carrier energy away from the probed volume, and simultaneously electron–phonon scattering transfers energy from the carriers to the vibrational modes on a timescale of about 7.6 ps. This leads to an increase in the energy available in the vibrational modes, which tends to increase the atomic position variance, but at the same time the re-hardening of the vibrational frequencies counteracts this to some extent. In addition, phonon–phonon interactions, which are necessary to establish thermodynamic equilibrium within the lattice, must also act to redistribute energy among the modes. Because measurements of the Debye–Waller factor from X-ray data offer only an average over all phonon modes, these measurements are not well suited to determine unambiguously whether the 'lattice temperature' is a well defined parameter at a particular time after excitation. One very interesting possibility for addressing this deficiency is to perform femtosecond time-resolved measurements of diffuse scattering away from Bragg reflections, which offers sensitivity to phonon momentum (Lindenberg *et al.*, 2008). Such measurements, possible only with the high fluxes to be available from linear-accelerator-based sources, offer the potential to more rigorously test models of electronically induced phonon softening and to measure the timescales on which local thermodynamic equilibrium of the lattice is achieved.

These experiments were performed on the X05LA beamline at the Swiss Light Source, Paul Scherrer Institut, Villigen, Switzerland. We thank D. Grolimund and C. Borca for outstanding assistance during experiments.

References

Aleksandrov, P. A., Afanas'ev, A. M. & Stepanov, S. A. (1984). *Phys. Status Solidi A*, **86**, 143–154.
Bartels, A., Dekorsy, T. & Kurz, H. (2000). *Phys. Rev. Lett.* **84**, 2981–2984.
Batterman, B. W. & Cole, H. (1964). *Rev. Mod. Phys.* **36**, 681–717.
Beaud, P., Johnson, S. L., Streun, A., Abela, R., Abramsohn, D., Grolimund, D., Krasniqi, F. S., Schmidt, T., Schlott, V. & Ingold, G. (2007). *Phys. Rev. Lett.* **99**, 174801.
Cavalieri, A. L. *et al.* (2005). *Phys. Rev. Lett.* **94**, 4.
Cucka, P. & Barrett, C. S. (1962). *Acta Cryst.* **15**, 865–872.
Eckstein, Y. (1960). *J. Appl. Phys.* **31**, 1534.
Fahy, S. & Reis, D. (2004). *Phys. Rev. Lett.* **93**, 109701.
Fischer, P., Sosnowska, I. & Szymanski, M. (1978). *J. Phys. C*, **11**, 1043–1051.
Fritz, D. M. *et al.* (2007). *Science*, **315**, 633–636.
Garrett, G., Albrecht, T., Whitaker, J. & Merlin, R. (1996). *Phys. Rev. Lett.* **77**, 3661–3664.
Glauber, R. (1963). *Phys. Rev.* **131**, 2766–2788.
Hase, M., Kitajima, M., Nakashima, S. & Mizoguchi, K. (2002). *Phys. Rev. Lett.* **88**, 067401.
Hase, M., Mizoguchi, K., Harima, H., Nakashima, S. & Sakai, K. (1998). *Phys. Rev. B*, **58**, 5448–5452.
Holldack, K., Khan, S., Mitzner, R. & Quast, T. (2006). *Phys. Rev. Lett.* **96**, 054801.
Hu, X. & Nori, F. (1997). *Phys. Rev. Lett.* **79**, 4605–4608.
Johnson, S. L., Beaud, P., Milne, C. J., Krasniqi, F. S., Zijlstra, E. S., Garcia, M. E., Kaiser, M., Grolimund, D., Abela, R. & Ingold, G. (2008). *Phys. Rev. Lett.* **100**, 155501.
Johnson, S. L., Beaud, P., Vorobeva, E., Milne, C. J., Murray, É. D., Fahy, S. & Ingold, G. (2009). *Phys. Rev. Lett.* **102**, 175503.
Lindenberg, A. M. *et al.* (2005). *Science*, **308**, 392–395.
Lindenberg, A. M. *et al.* (2008). *Phys. Rev. Lett.* **100**, 5.
McNeil, B. (2009). *Nature Photonics*, **3**, 375–377.
Merlin, R. (1997). *Solid State Commun.* **102**, 207–220.
Merlin, R. (2009). Personal communication.
Misochko, O. V., Ishioka, K., Hase, M. & Kitajima, M. (2006). *J. Phys. Condens. Mater.* **18**, 10571–10584.
Murray, É. D., Fahy, S., Prendergast, D., Ogitsu, T., Fritz, D. M. & Reis, D. A. (2007). *Phys. Rev. B*, **75**, 184301.
Murray, É. D., Fritz, D. M., Wahlstrand, J., Fahy, S. & Reis, D. A. (2005). *Phys. Rev. B*, **72**, 060301(R).
Narayana, M. S. & Krishna, N. G. (2005). *Phys. Status Solidi A*, **202**, 2731–2736.
Peierls, R. E. (1991). *More Surprises in Theoretical Physics*. Princeton University Press.
Rousse, A., Rischel, C. & Gauthier, J.-C. (2001). *Rev. Mod. Phys.* **73**, 17–31.
Schoenlein, R., Chattopadhyay, S. & Chong, H. (2000). *Science*, **287**, 2237–2240.
Schoenlein, R., Leemans, W. & Chin, A. (1996). *Science*, **274**, 236–238.
Sciaini, G., Harb, M., Kruglik, S. G., Payer, T., Hebeisen, C. T., zu Heringdorf, F.-J. M., Yamaguchi, M., von Hoegen, M. H., Ernstorfer, R. & Miller, R. J. D. (2009). *Nature (London)*, **458**, 56–59.

Sokolowski-Tinten, K., Blome, C., Blums, J., Cavalleri, A., Dietrich, C., Taraevitch, A., Uschmann, I., Förster, E., Kammler, M., von Hoegen, M. H. & von der Linde, D. (2003). *Nature (London)*, **422**, 287–289.

Sokolowski-Tinten, K., Blome, C., Dietrich, C., Tarasevitch, A., von Hoegen, M., von der Linde, D., Cavalleri, A., Squier, J. A. & Kammler, M. (2001). *Phys. Rev. Lett.* **87**, 225701.

Stevens, T., Kuhl, J. & Merlin, R. (2002). *Phys. Rev. B*, **65**, 144304.

Thomsen, C., Grahn, H., Maris, H. & Tauc, J. (1986). *Phys. Rev. B*, **34**, 4129–4138.

White, G. (1972). *J. Phys. C*, **5**, 2731–2745.

Zeiger, H. J., Vidal, J., Cheng, T. K., Ippen, E. P., Dresselhaus, G. & Dresselhaus, M. S. (1992). *Phys. Rev. B*, **45**, 768–778.

Zijlstra, E. S., Tatarinova, L. & Garcia, M. (2006). *Phys. Rev. B*, **74**, 220301(R).